AIAA JOURNAL
Vol. 58, No. 8, August 2020

Localization of Swept Free-Tip Airfoil Noise Sources by Microphone Array Processing

Gyuzel R. Yakhina* and Michel Roger†
University of Lyon, 69134 Ecully, France
Arthur Finez,‡ Simon Bouley,‡ and Valentin Baron§
MicrodB, 69130 Ecully, France
Stéphane Moreau¶
University of Sherbrooke, Sherbrooke, Quebec J1K2R1, Canada
and
Justine Giez**
Safran Aircraft Engines, 77500 Moissy-Cramayel, France

https://doi.org/10.2514/1.J058231

A postprocessing methodology of microphone-array results for accurate source localization and separation is described. A method constrained iterative restoration algorithm with an assumption of uncorrelated sources is used to extract quantitative spectral results for multiple noise sources identified on a wall-mounted finite-span swept and cambered airfoil tested in an open-jet aeroacoustic facility. This allows understanding of the contribution of each source in the noise generation process. The total sound pressure level is reconstructed from the individual spectra of each noise source and extrapolated in the far field to be compared with a single-microphone spectrum. The Bayesian algorithm is used to improve the comparison between reconstructed and experimental spectra because it takes into account the coherent nature of the sources. The analytical models of the source mechanisms and of their spanwise correlation are proposed as a tool to define future improvements.

Nomenclature

A_0	=	reference area
b	=	beamforming output
$\boldsymbol{b}$	=	vector of beamforming map
b_F	=	focalization output
$\mathcal{C}$	=	cone of positive semidefinite matrices
c	=	chord length
c_0	=	speed of sound
$\mathcal{D}^+$	=	set of diagonal matrices having positive or null elements
E	=	Fresnel integral
f	=	frequency
G	=	two-dimensional free-space Green's function
H	=	matrix of steering vectors
$H_\lambda^\dagger$	=	regularized pseudoinverse of matrix H
$\boldsymbol{h}$	=	vector of the propagation model from the focus point to the microphones
$\boldsymbol{h}_{FF}$	=	propagation vector from the source point set to the far-field microphone
k, k_1	=	acoustic and aerodynamic wave numbers
L	=	span length
$\mathcal{L}$	=	analytical radiation transfer function
L_p	=	sound pressure level
l	=	norm
$\ell(y_1)$	=	unsteady lift distributed along the airfoil
ℓ_y	=	spanwise correlation length
M_0	=	mean flow Mach number
N	=	number of fast Fourier transform bins or number of eigenvalues N_m
N_m	=	number of microphones
N_s	=	number of steering vectors $\boldsymbol{h}$
$\boldsymbol{p}$	=	vector containing the measured data at specific frequency
$\boldsymbol{q}$	=	source amplitude vector
R	=	radius of the sphere
r_i	=	Euclidean distance between the scan point and the microphone i
S_{pp}	=	power spectral density of far-field acoustic pressure
$\boldsymbol{S}_{pp}$	=	measurement covariance matrix at a given frequency (also called microphone cross-spectral matrix)
$\boldsymbol{S}_{qq}$	=	source covariance matrix at a given frequency (also called source cross-spectral matrix)
S_{uu}	=	streamwise velocity power spectral density
S_{ww}	=	upwash-velocity power spectral density
S_0	=	convection-corrected distance
s_i	=	ith diagonal element of $\tilde{\boldsymbol{S}}_{qq}$
s_{pp}	=	sound power level
T_r	=	matrix trace
t	=	time
U_0	=	mean flow velocity
w	=	amplitude of the incident velocity fluctuations at ω
(x_1, x_2, x_3)	=	coordinates for observer
(y_1, y_2)	=	coordinates for the source with origin at midchord
α	=	angle of attack
Γ	=	array response matrix
Δx	=	size of the discretization mesh cell
Λ	=	turbulence integral length scale
$\Lambda_{\max}$	=	the greatest eigenvalue of matrix H
λ	=	regularization parameter
μ	=	convergence parameter
ρ_0	=	mean flow density
ω	=	angular frequency

Presented as Paper 2018-3935 at the 2018 AIAA/CEAS Aeroacoustics Conference, Atlanta, GA, June 25–29, 2018; received 21 January 2019; revision received 3 March 2020; accepted for publication 10 April 2020; published online 15 May 2020.

*Postdoctoral Student, Fluid and Acoustic Mechanics Laboratory, UMR CNRS 5509, 36 Avenue Guy de Collongue.
†Professor, Fluid and Acoustic Mechanics Laboratory, UMR CNRS 5509, 36 Avenue Guy de Collongue.
‡Acoustic Engineer, 28 Chemin du Petit Bois.
§Ph.D. Candidate, 28 Chemin du Petit Bois.
¶Professor, Depart. Génie Mécanique, 2500 Boulevard de l'Université. Lifetime Member AIAA.
**Ph.D. Candidate, Aerodynamics and Acoustics Department, Rond-Point René Ravaud-Réau.

Superscripts

(k)	=	value at kth iteration
$*$	=	conjugate transpose operator
$\sim$	=	estimated quantity computed from sound source-localization algorithm

I. Introduction

IN MOST experiments investigating airfoil noise from far-field measurements using single microphones, which are typically performed in open-jet anechoic wind tunnels, two main issues are identified. First, the noise from the tested airfoil is contaminated by some background noise generally caused by the nozzle jet mixing and the interaction of the jet with other surfaces such as endplates. Usually, this background noise is assumed to be uncorrelated with the targeted airfoil noise and is measured separately without an airfoil so that it can be subtracted from the noise measured with the airfoil installed [1,2]. This makes extraction impossible when airfoil noise is masked by the background noise, and consequently reduces the frequency range of investigation. Second, airfoil noise itself is the result of multiple noise source contributions, such as turbulence-interaction noise at the leading edge, trailing-edge noise, tip-vortex associated noise, and possibly leading-edge vortex-induced noise [3,4]. The two latter mechanisms are clearly observed in experiments with a free airfoil tip of significant sweep and loading, which is the case in the present work, as detailed in Sec. IV. Additional noise sources could also be present in the near wake when the Mach number is increased, as recently evidenced by Wu et al. [5] on the controlled diffusion airfoil. The single-microphone measurements do not allow separating these different contributions, which is a serious issue whenever more than one mechanism contributes to the noise.

The far-field microphones allow measuring the radiated sound and its directivity. Completing these far-field measurements with microphone-array localization techniques that can be used to separate the sources and to provide quantitative estimates of each of them is of primary interest. Several methods such as classical beamforming [6], De-convolution Approach for the Mapping of Acoustic Sources (DAMAS) [7], and CLEAN-Source Coherence (SC) [8], for instance, have been developed. Yet, the accuracy of such noise source extraction methodologies and the practical issues inherent to the localization algorithms used are seldom addressed in the literature. The recent AIAA benchmark [9,10] dedicated to testing various array-processing methods on synthetic signal and actual measurements showed that there was not any perfect method and, depending on the parameters of sources, one could provide more reasonable results than another. Therefore, the appropriate source-localization method should be chosen for the particular case studied so that physical features of the generated noise sources are taken into account.

The present study deals with the application of several known source-localization methods: not only to detect but also to quantify multiple noise sources of the swept-finite airfoil. The source-localization studies of the leading- [11] and trailing-edge [12,13] noise sources were conducted previously in a classical setup with the airfoil held between two endplates. However, as was pointed out in previous works [14,15], the flow around the wall-mounted finite length airfoil is three-dimensional, and additional noise sources such as airfoil tip vortices can contribute to the process [16], especially at high effective angles of attack. The results of the source localization with the beamforming method reported in Refs. [14,15] show the existence of a junction noise source at low frequencies, increasing with the angle of attack; a trailing-edge noise source dominating at middle frequencies for low angles of attack; and a trailing-edge tip source observed at high frequencies.

The present study is also part of a project focused on broadband-noise mechanisms involved in contrarotating open rotors. The acoustic and aerodynamic measurements for a wall-mounted finite-span swept airfoil have been conducted at the École Centrale de Lyon (ECL), and some preliminary results have been presented by Giez et al. [3,4]. Several angles of attack were tested in clean flow and a turbulent stream to have different physical effects, such as a leading-edge vortex and a leading-edge turbulence impingement. The present work proposes an advanced analysis of the source-localization results. First, the cross-spectral matrix fitting method called the constrained iterative restoration algorithm (CIRA) [17] is compared to a focalization algorithm and is used to calculate the power of individual noise sources. The comparison between the calculated noise spectrum with the far-field single-microphone measurement shows some discrepancies at low frequencies that might be attributed to the assumption of uncorrelated noise sources in the CIRA method. To improve the calculated spectrum, the iterative Bayesian focusing [18] algorithm based on the Bayes rule is applied. This method allows including the coherence of the sources into the reconstruction process. Beyond the need to properly characterize the individual sources and their ranking as a function of the configuration, the study is also meant to build a database for each of them in view of the validation of analytical and numerical predictions for various mechanisms. One of the dominant mechanisms is the leading-edge noise produced by impinging turbulence. The analytical model of the leading-edge noise based on Amiet's theory was developed for the swept airfoil. The interest of the turbulence-interaction noise model is that it provides a theoretical expression for the correlation length of the sources: once tuned on measured velocity fluctuations. It is used to stress the underlying issue related with the assumption of uncorrelated sources in some microphone-array postprocessing techniques.

Section I describes the experimental setup with the finite swept airfoil at the ECL. Section II presents an analytical model for the leading-edge turbulence-interaction noise, which assessed estimates of the noise source correlation length. Section III outlines the postprocessing techniques, such as conventional beamforming, cross-spectral matrix fitting CIRA, and iterative Bayesian focusing algorithms. Section IV shows source-localization maps produced by the first two aforementioned methods, spectra provided by the CIRA method for separated noise sources observed at various flow conditions, and comparison of the reconstructed spectra by CIRA and iterative Bayesian focusing methods with measured far-field spectra. Finally, some conclusions are drawn.

II. Experimental Setup

A series of experiments has been carried out in the large open-jet anechoic wind tunnel of the École Centrale de Lyon with a converging nozzle with a 300×400 mm rectangular section. The flow is delivered by a subsonic centrifugal fan, and the residual turbulence intensity is 0.5%. An additional grid that generates a turbulence intensity of 8% is used to investigate turbulence-interaction noise more specifically. The flow speed ranges from 30 to 100 m/s (chord-based Reynolds numbers from 2.9×10^5 to 11×10^5, and a maximum Mach number close to 0.3) [3,4].

A swept cambered airfoil with a chord length of 150 mm, a span length of 250 mm, a sweep angle of 35 deg, and a relative thickness of 4% with a free tip is mounted on a single endplate. A rotating disk allows varying of the geometrical angle of attack from 0 to 11 deg. The airfoil/plate junction at the leading edge is located 200 mm downstream of the wind-tunnel nozzle, and the whole mockup is embedded well inside the potential core of the jet so that the direct interaction with the jet shear layers is avoided. It must be noted that the convection effect and the refraction that occurs across the shear layers of the wind-tunnel jet are corrected in the postprocessing described in Sec. III. Far-field single-microphone measurements are made normal to the mockup 2 m away from the leading edge in the midspan plane. A piezotronic type 426B03 quarter-inch microphone is used.

The microphone array used for source localization is made of 81 digital Micro Electro Mechanical Systems (MEMS) microphones arranged in a nine-arm spiral structure covering a circular surface of 0.6 m in diameter developed by MicrodB (Fig. 1). It is placed at a normal distance of 50 cm from the airfoil outside of the flow (Figs. 2 and 3). The localization is made on both airfoil sides: test 1 was for the phased array facing the suction side of the airfoil, and test 2 was for the phased array facing its pressure side. For each experimental configuration, the signals of all probes are simultaneously recorded by the National Instruments multichannel acquisition system. It is worth noting that the far-field measurements (test 3 in Fig. 2) and source-localization measurements were not conducted simultaneously.

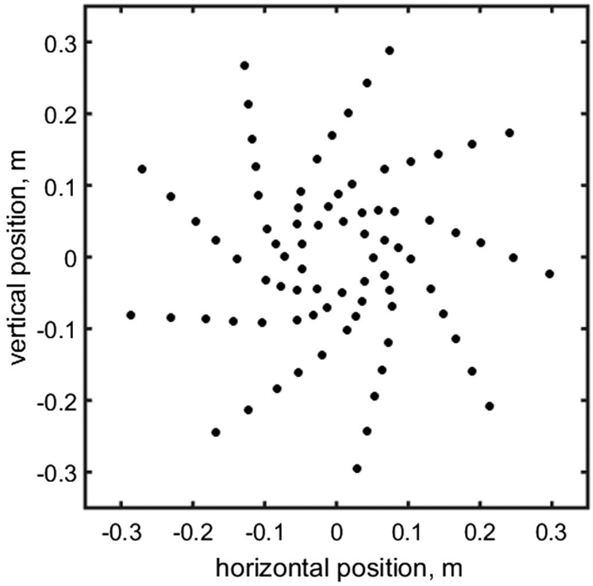

Fig. 1 Scheme of the microphone array.

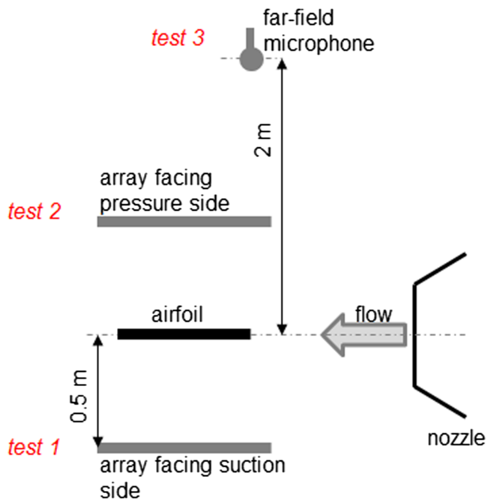

Fig. 2 Sketch of top view of experimental setup (not scaled). Three tests conducted: test 1) measurements with microphone array facing suction side, test 2) measurements with microphone array facing pressure side, and test 3) far-field measurements.

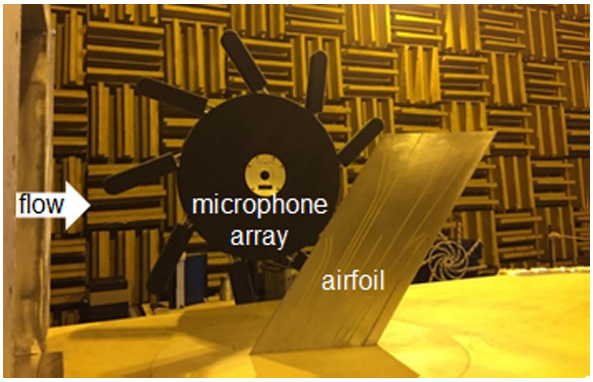

Fig. 3 Photograph of experimental setup: top view.

Therefore, the microphone array did not interfere with the far-field acoustic measurements. From the point of view of the airfoil, the array and the far-field microphone are located approximately in the same direction.

The use of MEMS microphones in a flat array raises an expected high-frequency artefact. Each microphone is mounted in a small cavity that induces a resonance around 18 kHz. This effect has been pointed out by Humphreys et al. [19]. The resonance needs to be corrected via a calibration procedure. A typical microphone response curve is presented in Fig. 4, showing the resonance in the high-frequency range. A correction filter is also shown; it is used to partially compensate for the resonance effect for frequencies below 18 kHz.

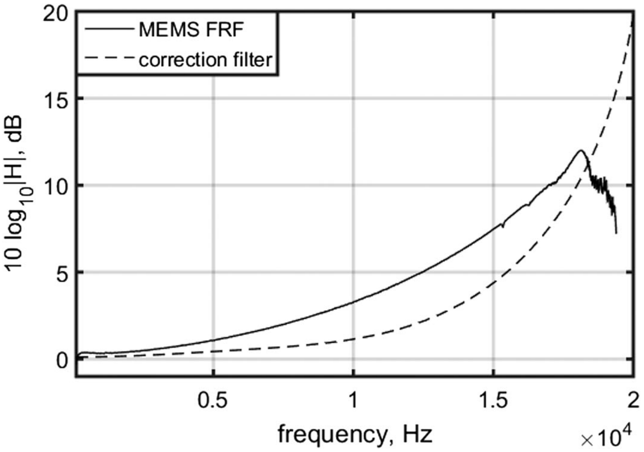

Fig. 4 Typical response curve of a microphone of the phased array, showing the high-frequency resonance.

Thus, when used for noise source strength quantification, the recommended use of the array is limited to frequencies below 10 kHz. However, this work investigates exploratory ways to study airfoil noise, including the very high-frequency range. Thus, source maps are shown above 10 kHz, even though this is beyond the operational frequency range recommended by the array manufacturer. The corresponding estimated error can reach 5 dB between 10 and 17 kHz and 10 dB between 17 and 20 kHz.

III. Analytical Model of Leading-Edge Noise

Analytical models, if available, provide a clear understanding of basic features that help with the interpretation of the noise source-localization results. Amiet's model of sound generation by interaction of vortical disturbances on a leading edge is discussed in this section, mostly in connection with high-frequency airfoil-noise sources. Such sources are clearly apparent in the source maps produced by the microphone-array postprocessing in the present study with grid-generated turbulence. Yet, they can hardly be extracted from the background noise in the high-frequency part of the spectrum when investigated with a single far-field microphone.

Amiet's model of turbulence-interaction noise at a leading edge is chosen here because it has proven its efficiency in predicting the broadband noise of thin airfoils [20–23]. For convenience, it is first considered in a two-dimensional context, assimilating the airfoil to a thin rigid segment of chord c embedded in a parallel uniform mean flow of speed U_0. The model allows deriving a closed-form expression for the unsteady lift $\ell(y_1)$ distributed along the airfoil chord by making use of the Schwarzschild technique [24,25]. This distribution corresponds to perfectly correlated equivalent dipoles at the considered frequency, in the usual sense of the acoustic analogy [26]. It reads

$$\ell(y_1) = \frac{2\rho_0 U_0 w \mathrm{e}^{\mathrm{i}\pi/4}}{\sqrt{\pi(1+M_0)k_1 y_1}} \mathrm{e}^{\mathrm{i}(1-M_0)(kc/2\beta^2)(1+2y_1/c)} \times\left\{1-\sqrt{\frac{2}{1+2y_1/c}}-E\left(\frac{kc}{\beta^2}(1-2y_1/c)\right)\right\} \tag{1}$$

in which y_1 is the chordwise coordinate with an origin at midchord; ρ_0 and U_0 are the mean flow density and speed; w is the amplitude of the incident upwash-velocity fluctuations normal to the airfoil at angular frequency ω; $k = \omega/c_0$ and $k_1 = \omega/U_0$ are the acoustic and aerodynamic wave numbers, respectively; $M_0 = U_0/c_0$; and $\beta^2 = 1 - M_0^2$. E is the Fresnel integral

$$E(\xi) = \int_0^{\xi} \frac{e^{it}}{\sqrt{2\pi t}}\,dt$$

In two dimensions, the sound radiation of the lift distribution can be computed numerically by making the scalar product with the normal derivative of the two-dimensional free-space Green's function in a uniformly moving fluid. This function, with the present convention $e^{i\omega t}$ for the time Fourier transform, is written as

$$G(x, y) = \frac{i}{4\beta} e^{-ikM_0(x_1-y_1)/\beta^2} H_0^{(1)}\left(\frac{kr_s}{\beta^2}\right) \qquad (2)$$

with $r_s^2 = (x_1 - y_1)^2 + \beta^2(x_2 - y_2)^2$. Here, $\boldsymbol{x} = (x_1, x_2)$ is the observer point and $\boldsymbol{y} = (y_1, y_2 = 0)$ is the source point.

Typical instantaneous pressure fields reconstructed this way are shown in Fig. 5. At 2 kHz, the chord length is in the same order of magnitude as the wavelength and the theory predicts distributed sources (in essence coherent all along the chord), which are not strongly concentrated at the leading edge. This distributed character corresponds to wave fronts neither clearly originating from the leading edge nor looking like spherical wave fronts. This suggests that an algorithm based on distributed uncorrelated monopoles that have spherical wave fronts will not precisely localize the source. Moreover, the trailing-edge noise also contributes in the experiment, with the same distributed character of theoretical sources (same Green's function) and similar wave front patterns concentrating only moderately at the trailing edge; whereas the theoretical wave fronts only refer to leading-edge noise. Apart from the wave front shift due to convection, both sources have nearly symmetrical radiating properties. Both sources of trailing-edge noise and leading-edge noise can hardly be discriminated with microphone-array algorithms at "relatively" low values of kc. Figure 5 illustrates the difficulty of localization at a precise point at 2 kHz. However, at 10 kHz (and for lower values), the chord covers several wavelengths. Therefore, two sources can be identified by algorithms at high frequencies, independent of the fact that the resolution possibly depends on the applied postprocessing technique.

Amiet's model also provides an expression for the far-field sound pressure Power Spectral Density (PSD). In the simple case of a rectangular airfoil of large aspect ratio, and for an observer in the midspan plane, this PSD reads

$$S_{pp}(\boldsymbol{x}, \omega) = \left(\frac{\rho_0 k c x_3}{2S_0^2}\right)^2 \pi U_0 \frac{L}{2} \Phi_{ww}(k_1, 0) |\mathcal{L}(x_1, k_1, 0)|^2 \qquad (3)$$

with

$$\Phi_{ww}(k_1, 0) = \frac{U_0}{\pi} S_{ww}(\omega) l_y(\omega)$$

where $S_{ww}(\omega)$ is the upwash-velocity spectrum, and $\ell_y(\omega)$ is the associated correlation length. $\mathcal{L}$ is an analytical transfer function, which is not detailed here. An extended version of this result accounting for sweep and other details was given by Giez et al. [3,4] and Quaglia et al. [27] but is not essential to the present discussion. It is enough to retain that the statistical quantities S_{ww} and ℓ_y of the incident turbulence determine the sound radiation. Once the complementary streamwise velocity spectrum S_{uu} is measured by hot-wire anemometry and properly fitted by a von Kármán or Liepmann model, an estimation of S_{ww} is obtained by assuming isotropy and sound predictions can be made [28]. The fitting in the present experiment generates values of the turbulent intensity and of the integral length scale Λ that are 8% and 2 cm, respectively. Also, $\ell_y(\omega)$ is deduced from Λ. Paterson and Amiet [21] pointed out that the spanwise correlation length of the induced lift on the airfoil is larger than the correlation length of the turbulence by typically a factor of about 1.6. Combined with the effect of sweep, this makes a factor of two reasonably expected in the present case.

The integral length scale Λ is 2 cm, which leads to the estimated spanwise correlation length reported in Fig. 6. More precisely, this length is made dimensionless by the 1 cm discretization step of the localization map, detailed later on and expressed in equivalent decibels. This rough analysis suggests that, beyond 4 kHz, the correlation length is smaller than the discretization step. This also occurs below 200 Hz but at so low frequencies the localization technique becomes less accurate and the jet noise becomes important. As long as the

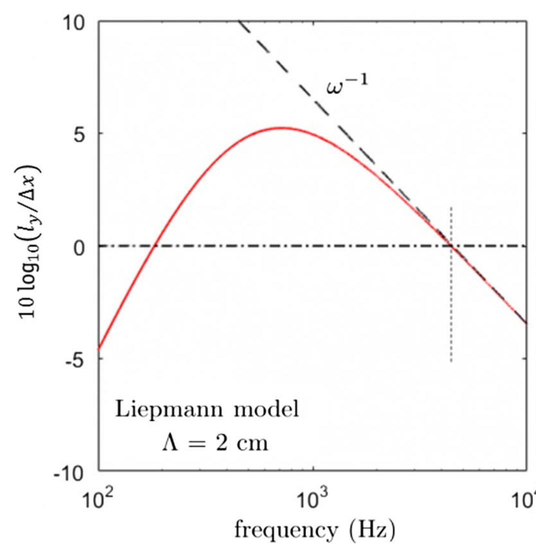

Fig. 6 Estimated ratio of spanwise correlation length to microphone-array discretization step $\Delta x = 1$ cm.

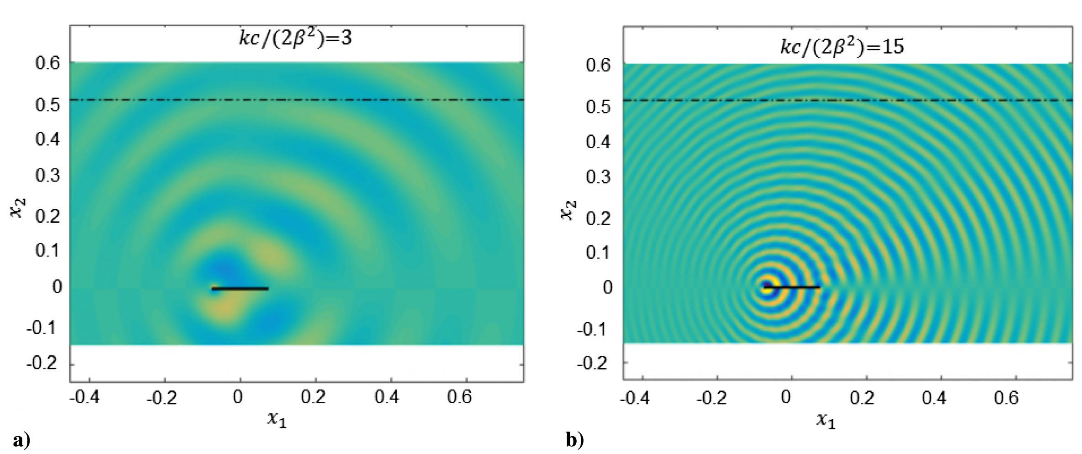

Fig. 5 Maps of typical instantaneous acoustic pressures radiated by an airfoil according to two-dimensional Amiet's model. High-frequency regime: a) 2 kHz and b) 10 kHz. Also, $c = 15$ cm and $U_0 = 90$ m/s, with typical array location along dashed–dotted line.

discretization step is larger than the correlation length, assuming uncorrelated cells in the localization is proper. Therefore, the source quantification can be used to reconstruct the far field in a convincing way, as will be presented in the next section. At frequencies for which the discretization step is smaller than the actual correlation length, the microphone-array postprocessing underestimates that length because adjacent cells are assumed uncorrelated. The approximation of Eq. (3) shows that the far-field predicted sound in the transposition procedure is also underestimated. When the ratio plotted in Fig. 6 is positive, it corresponds to the expected underestimate of the turbulence-interaction noise level; and its value can be used to somewhat empirically correct the far-field spectrum at low frequencies produced by the transposition procedure.

IV. Postprocessing Techniques

Three existing sound source-localization algorithms are used in the present investigation: the conventional beamforming [6], a cross-spectral matrix fitting method called the CIRA [17], and the Bayesian algorithm [18]. They are briefly presented in this section and compared to each other. For an exhaustive comparison with the literature, the interested reader should refer to the works of Leclére et al. [29] and Merino-Martinez et al. [30]. It is here intended to compare these three existing sound source algorithms under the light of the present aeroacoustic experiment and to evaluate their ability to estimate the acoustic spectrum at any observer position using array measurements. Of particular concern is the question of the source coherence length, which may produce biased estimates of acoustic spectra as explained in Sec. II. In this section, a time Fourier transform and an ensemble-averaging analysis are systematically applied as a preprocessing of all variables, and all variables except distances are functions of frequency. The presented algorithms are applied separately over the frequency range of interest.

A. Beamforming Algorithm

The conventional beamforming (CBF) algorithm [6] is a standard method used as a reference array-processing technique because of its robustness when comparing predictions to noise measurements and its limited computational cost. The main drawbacks are the low spatial resolution, especially at lower frequencies, and the poor dynamic range due to numerical artefacts known as side lobes.

Let N_m be the number of microphones in the array and $\boldsymbol{h}$ a complex $[N_m \times 1]$ vector representing the propagation model from the focus point to the microphones. The problem to be solved separately at each frequency is

$$\tilde{b} = \underset{b\in\mathbb{R}^+}{\arg\min}\|\boldsymbol{S}_{pp} - b\boldsymbol{h}\boldsymbol{h}^*\|_F^2 \tag{4}$$

where $\boldsymbol{S}_{pp}$ is the $[N_m \times N_m]$ measurement cross-spectral matrix, and b is the beamforming output. The quantity $b\boldsymbol{h}\boldsymbol{h}^*$ is a synthetic cross-spectral matrix (CSM) produced by an isolated source located at the scan point with a squared amplitude b and with a directivity pattern corresponding to $\boldsymbol{h}$. It is worth noting that $\boldsymbol{h}$ encompasses both characteristics of the source (as the directivity pattern) and propagation features. In most applications, the steering vector $\boldsymbol{h}$ is chosen as the three-dimensional (3-D) free-field Green's function, corresponding to a monopole, such that its elements are

$$h_m = \frac{e^{-ikr_i}}{4\pi r_i} \tag{5}$$

where r_i is the Euclidean distance between the scan point and microphone i, and k is the acoustic wave number. It is possible to modify the steering vector to include specific propagation effects as the convection of sound waves by a wind-tunnel flow. Convected distances [31] are used throughout this work instead of the Euclidean distance to this end.

It can be shown that the solution of Eq. (4) is

$$\tilde{b} = \frac{\boldsymbol{h}^*\boldsymbol{S}_{pp}\boldsymbol{h}}{|\boldsymbol{h}^*\boldsymbol{h}|^2} \tag{6}$$

From Eq. (6), it is clear that beamforming is a point-to-point process because the array must be successively pointed toward several scan points by means of a numerical change in the steering vector $\boldsymbol{h}$. Thus, each point of the grid is considered independently of its neighbors.

The strong single source assumption has several consequences: first, when several sources are present, energy leakage occurs from one focus position to another, and it is not possible to exactly recover the amplitude of any of the sources. This remark basically motivated the development of cross-spectral matrix fitting methods as presented in Sec. III.B. Second, the source correlation effects are not included in this simple model: nor is the possibility to depart from the directivity pattern expressed in $\boldsymbol{h}$. In the presence of spatially correlated sources, this can bring significant and uncontrolled discrepancies in power estimates using CBF.

For these reasons, the beamforming principle is not used in this study as a means to quantify aeroacoustic sources but only as a tool to localize the different regions of noise generation. Elias [32] formulated a localization problem instead of the quantification problem of Eq. (4) and obtained the following solution:

$$\tilde{b}_F = \frac{\boldsymbol{h}^*\boldsymbol{S}_{pp}\boldsymbol{h}}{|\boldsymbol{h}^*\boldsymbol{h}|T_r(S_{pp})} \tag{7}$$

where b_F is referred to as the "focalization" output to be distinguished from the beamforming output, and $T_r(S_{pp})$ is the matrix trace. Note that the difference between Eqs. (4) and (7) lies in the denominator power. It yields a different distance weighting for the monopole model of Eq. (5). In practice, this enhances the spatial resolution at the expense of a loss of quantitative estimation. In the following, the focalization indicator [Eq. (7)] will thus be used. It is worth noting that different normalizations of the steering vector were discussed by Sarradj [33].

Finally, in the beamforming and focalization algorithms, the diagonal removal process has been used, which basically ignores the diagonal terms of the vector matrix products in Eqs. (6) and (7). The purpose of the diagonal removal process is to minimize shear layer noise contamination, and it is now standard in microphone-array postprocessing in wind tunnels [31]. It is applied in this work in both the focalization and CIRA algorithms.

B. Cross-Spectral Matrix Fitting Algorithm

To overcome the limitations of beamforming in both resolution and the dynamic range, cross-spectral matrix fitting algorithms have been developed for aeroacoustics since 2000 for aeroacoustics [7,34]. The main idea is to replace the single source assumption by a distributed uncorrelated source assumption so that all sources are considered at once. Basically, the aim of the deconvolution method is to remove the blurring effects of the inverse operator from the source energy map. Those effects are defined by the point spread function of the array. While deconvolution problems are expressed in the beamforming map domain, the cross-spectral matrix fitting problem search for the source distribution amplitude that explains, at best, the measured CSM is then searched. Similar to Eq. (4), if the N_s steering vectors $\boldsymbol{h}$ are cast in a single $[N_m \times N_s]$ matrix H, the new problem formulation reads

$$\tilde{\boldsymbol{S}}_{qq} = \underset{S_{qq}\in\mathcal{D}^+}{\arg\min}\|\boldsymbol{S}_{pp} - \boldsymbol{H}\boldsymbol{S}_{qq}H^*\|_F^2 \tag{8}$$

where $\mathcal{D}^+$ represents the set of diagonal matrices having positive or null elements. Here and in the following, the H matrix consists of a set of arbitrary model vectors, representing any type of source directivity and propagation path. $\boldsymbol{S}_{qq}$ represents the source covariance matrix at a given frequency; it is forced to be diagonal in this class of algorithms. The quantity $\boldsymbol{H}\boldsymbol{S}_{qq}H^*$ is a synthetic CSM produced by the source distribution located on the scanning point set, with the amplitude specified in matrix $\boldsymbol{S}_{qq}$ and directivity patterns defined by the transfer matrix H. The positivity constraint $\mathcal{D}^+$ arises naturally from the fact that diagonal elements of $\tilde{\boldsymbol{S}}_{qq}$ are source autospectra.

Equation (8) is common to many cross-spectral matrix fitting algorithms like the Spectral Estimation Method (SEM) [34], Covariance Matrix Fitting approach (CMF) ([35] or [36]). The assumptions in deconvolution algorithms like DAMAS [7] are similar. The difference between these algorithms lies in the technique employed to find a (possibly not unique) solution. The version used in this work makes use of a constrained iterative restoration algorithm [37] to solve the problem described in Ref. [36]. The method is explained in the following. It has been chosen because of its good convergence performances. In the end, all aforementioned deconvolution and cross-spectral matrix fitting algorithms are expected to yield similar results, provided that the same convergence criteria are used.

The beamforming outputs b for all candidate source positions are gathered in a $[N_s \times 1]$ vector $\boldsymbol{b}$ called the beamforming map. Let $\boldsymbol{\Gamma}$ be the $[N_s \times N_s]$ array response matrix defined by

$$\Gamma_{ij} = \frac{\sum_{m=1}^{N_m}\sum_{n=1}^{N_m} H_{mj}H_{mi}^*H_{ni}H_{nj}^*}{\sum_{m=1}^{N_m}\sum_{n=1}^{N_m} |H_{mj}|^2|H_{nj}|^2} \tag{9}$$

Let us also $s_i^{(k)}$ denote the ith diagonal element of $\tilde{\boldsymbol{S}}_{qq}$ $(i = 1 \ldots N_s)$ at iteration k. These values are assembled in a $[N_s \times 1]$ vector $\boldsymbol{s}^{(k)}$.

The initialization is $s_i^{(0)} = 0$ for all sources i. At each k iteration, the first step is to compute the error vector between the initial CBF map $\boldsymbol{b}$ and a modeled beamforming map $\boldsymbol{\Gamma}s^{(k-1)}$ produced by the source distribution found at the previous iteration:

$$\boldsymbol{e}^{(k)} = \boldsymbol{b} - \boldsymbol{\Gamma}s^{(k-1)} \tag{10}$$

Then, the solution is updated from the computed error:

$$\boldsymbol{s}^{(k)} = \boldsymbol{s}^{(k-1)} + \mu\boldsymbol{e}^{(k)} \tag{11}$$

where μ is a user-defined convergence parameter that controls the weight given to the error in the solution update; it ensures the algorithm stability. Parameter μ has to be chosen as large as possible to maximize the convergence speed. However, high values can lead to severe oscillations during the iteration process, preventing convergence. A critical value for μ is thus sought, which produces the highest convergence speed while keeping the algorithm stable. Noting that the combination of Eqs. (10) and (11) yields an arithmetic–geometric sequence, a convergence radius can be derived:

$$\mu = \frac{2}{\Lambda_{\max}} \tag{12}$$

where $\Lambda_{\max}$ is the greatest eigenvalue of matrix H. At each iteration, the partial solution is constrained to positive values: $s_i^{(k)} = 0$ if $s_i^{(k)} < 0$. Computations are stopped when the threshold for the relative error (10^{-4}) is reached or when a large number of iterations (1000) has been computed.

Deconvolution and cross-spectral matrix fitting algorithms are known to provide a much better spatial resolution and dynamic range than conventional beamforming and focalization formulations [8–10]. Regarding coherence length considerations, the sources are perfectly uncorrelated in the cross-spectral matrix fitting model because $\tilde{\boldsymbol{S}}_{qq}$ is required to be diagonal in Eq. (8). If spatial correlation exists in the physical situation with a physical coherence length ℓ_y, the source correlation features will not be reproduced correctly by $\tilde{\boldsymbol{S}}_{qq}$. It is expected that the radiated field of the estimated sources will be similar to the field radiated by a source distribution exhibiting a coherence length $\tilde{\ell}_y$ close to the chosen discretization mesh size $\tilde{\ell}_y \simeq \Delta x$. When $\tilde{\ell}_y$ is different from ℓ_y, biases in source power estimates could occur using the CIRA algorithm as a consequence of the error analysis in the coherence length shown in Fig. 6. One of the goals of Sec. IV is to quantify these errors from experimental data in various coherence length configurations.

C. Iterative Bayesian Focusing

Other postprocessing algorithms do not use the assumption of uncorrelated sources and are more likely to deal with spatial correlation effects. A first example is the DAMAS-C [38] algorithm, which solves the following problem:

$$\tilde{\boldsymbol{S}}_{qq} = \underset{\boldsymbol{S}_{qq}\in\mathcal{C}}{\arg\min}\|\boldsymbol{S}_{pp} - \boldsymbol{H}\boldsymbol{S}_{qq}H^*\|_F^2 \tag{13}$$

where $\mathcal{C}$ is the cone of positive semidefinite matrices; $\boldsymbol{S}_{qq} \in \mathcal{C}$ specifies that $\boldsymbol{S}_{qq}$ is Hermitian or "CSM-like." Unlike Eq. (8), this formulation allows taking into account the correlation length, as was mentioned by Fleury et al. [39] and Fleury and Davy [40], because off-diagonal values of $\tilde{\boldsymbol{S}}_{qq}$ are not forced to be null. However due to its large computational cost, DAMAS-C has limited experimental applications [30].

Another class of coherence compatible algorithms is inverse techniques [41,29]; they involve a pseudoinversion of the transfer matrix H. Generalized Inverse Beamforming (GIB) [42], Inverse Frequency Response Function (iFRF) [43], and Bayesian focusing [18] all belong to this group of methods. Rather than stating the mathematical formulation in a quadratic form as in Eq. (13), a linear form is used:

$$\tilde{\boldsymbol{q}} = \underset{\boldsymbol{q}\in\mathbb{C}^n}{\arg\min}\|\boldsymbol{p} - \boldsymbol{H}\boldsymbol{q}\|_2^2 + \lambda^2\|\boldsymbol{q}\|_\ell^\ell \tag{14}$$

where $\boldsymbol{p}$ is a $[N_m \times 1]$ vector containing the measured data at a specific frequency; it typically contains the complex pressure values of a fast Fourier transform (FFT) snapshot with index i over the set of microphones, or one of the principal components (eigenvector scaled by its corresponding eigenvalue square root) of the measured CSM. In Eq. (14), the first term $\|\boldsymbol{p} - \boldsymbol{H}\boldsymbol{q}\|_2^2$ represents the residue in the pressure data fitting, which is a linear variation of the quadratic argument term in Eq. (13). The second term $\lambda^2\|\boldsymbol{q}\|_l^l$ is a penalization term on the solution l norm. It helps avoid stability problems due to a possible low conditioning of matrix H. The norm $0 \le l \le 2$ is known to force the solution sparsity for the smallest l values. The balance between the two terms is given by the regularization parameter λ, which must be chosen with care and be in agreement with the signal-to-noise ratio in the measurements. $\boldsymbol{S}_{pp}$ is linked to $\boldsymbol{p}_i$ through

$$\boldsymbol{S}_{pp} = \frac{1}{\kappa(N)}\sum_{i=1}^{N}\boldsymbol{p}_i\boldsymbol{p}_i^* \tag{15}$$

where N is either the number of FFT bins or the number of eigenvalues N_m. Also, $\kappa(N) = N$ in the first case and $\kappa(N) = 1$ in the second one. Similarly, once the N source amplitude vector estimates $\tilde{\boldsymbol{q}}_i$ $(i = 1 \ldots N)$ are found, the source CSM can be estimated:

$$\tilde{\boldsymbol{S}}_{qq} = \frac{1}{\kappa(N)}\sum_{i=1}^{N}\tilde{\boldsymbol{q}}_i\tilde{\boldsymbol{q}}_i^* \tag{16}$$

To find solutions $\tilde{\boldsymbol{q}}_i$ of Eq. (14), Antoni [18] proposed the Bayesian focusing algorithm. It is based on a statistical approach of the sound source reconstruction problem given by Eq. (14) with $l = 2$. The algorithm involves the computation of a regularized pseudoinverse $H_\lambda^\dagger$ of matrix H. The choice of the regularization parameter λ employs an empirical technique [44], and thus depends on $\boldsymbol{S}_{pp}$. Others steps of $H_\lambda^\dagger$ computation only use model information contained in H and prior matrices. Details of the resolution are not given in this paper. The interested reader should refer to Refs. [18,44–46]. Once $H_\lambda^\dagger$ is calculated, it is actually not useful to compute explicitly $\boldsymbol{p}_i$ and $\tilde{\boldsymbol{q}}_i$; the estimated source CSM is directly linked to $\boldsymbol{S}_{pp}$ and $H_\lambda^\dagger$:

$$\tilde{S}_{qq} = H_\lambda^\dagger S_{pp} H_\lambda^{\dagger *} \tag{17}$$

A specific aspect of the Bayesian focusing is the possibility to incorporate it in an iterative process so that the spatial resolution is gradually refined [45,46] because it is equivalent to solving Eq. (14) with a lower l value, thereby enforcing the sparsity of the solution. In the meantime, the hyperdirectivity of the reconstructed sound field toward the array, which is a known drawback of the least-square solution of the linear equation [Eq. (14)] is also significantly reduced. This last point helps to predict the sound pressure at positions where the array microphone is absent, as will be shown in Sec. IV. The iterative Bayesian focusing (IBF) with 30 iterations has been applied in the present work. This visually provides a good compromise between the spatial resolution improvement and the preservation of the extended nature of the sources.

Another particular feature of this algorithm is its ability to include prior knowledge on the source position, on the source correlation, and on the possible correlation with extraneous noise sources. However, this feature is not used in the present study, and all prior correlation matrices are set to unity.

Since $\tilde{S}_{qq}$ is not required to be a diagonal matrix, inverse methods are well suited to provide information on the source correlation from the off-diagonal values, such as an estimate of the source coherence function that depends on the source spacing and the frequency. The physical validity of this information is still a matter of research and is one of the topics of this work. Nonetheless, it is expected that IBF is less sensitive to the power estimate errors described in the previous section than the CBF and CIRA: especially in cases where $\ell_y > \Delta x$.

V. Source-Localization Results

The present section shows the comparison of source-localization maps provided by focalization and CIRA methods. The far-field sound pressure level spectra reconstructed for each noise source by the CIRA method are summed and compared with the far-field measured spectrum. The Bayesian method is used to improve the reconstruction spectrum. All calculations have been done for 5 s signals at frequencies ranging from 0.2 to 20 kHz. The frequency resolution is 10 Hz with a sample overlap of 50%. The discretization step of the localization map is 0.01 m.

The beamforming technique applied in previous work [4] showed that several noise sources can be observed, depending on the configuration and the frequency range: 1) the interaction with the boundary layer at the junction of the airfoil with the plate, 2) the airfoil tip section where the tip vortex develops, 3) the leading-edge turbulence interaction, 4) the scattering of boundary-layer turbulence at the trailing edge, and 5) special sources associated with the formation of a leading-edge vortex.

Various configurations with different angles of attack and turbulence intensities were selected to characterize each source. The most detailed investigation was done with the CIRA method, which allows us to separate the sources and to obtain quantitative estimates of the associated spectra. The acoustic levels are presented with respect to some reference level (RL).

Figure 7 shows the localization maps calculated by the focalization and by the CIRA method for the configuration at a 9 deg angle of attack and 90 m/s with a residual turbulence intensity of 0.5%.

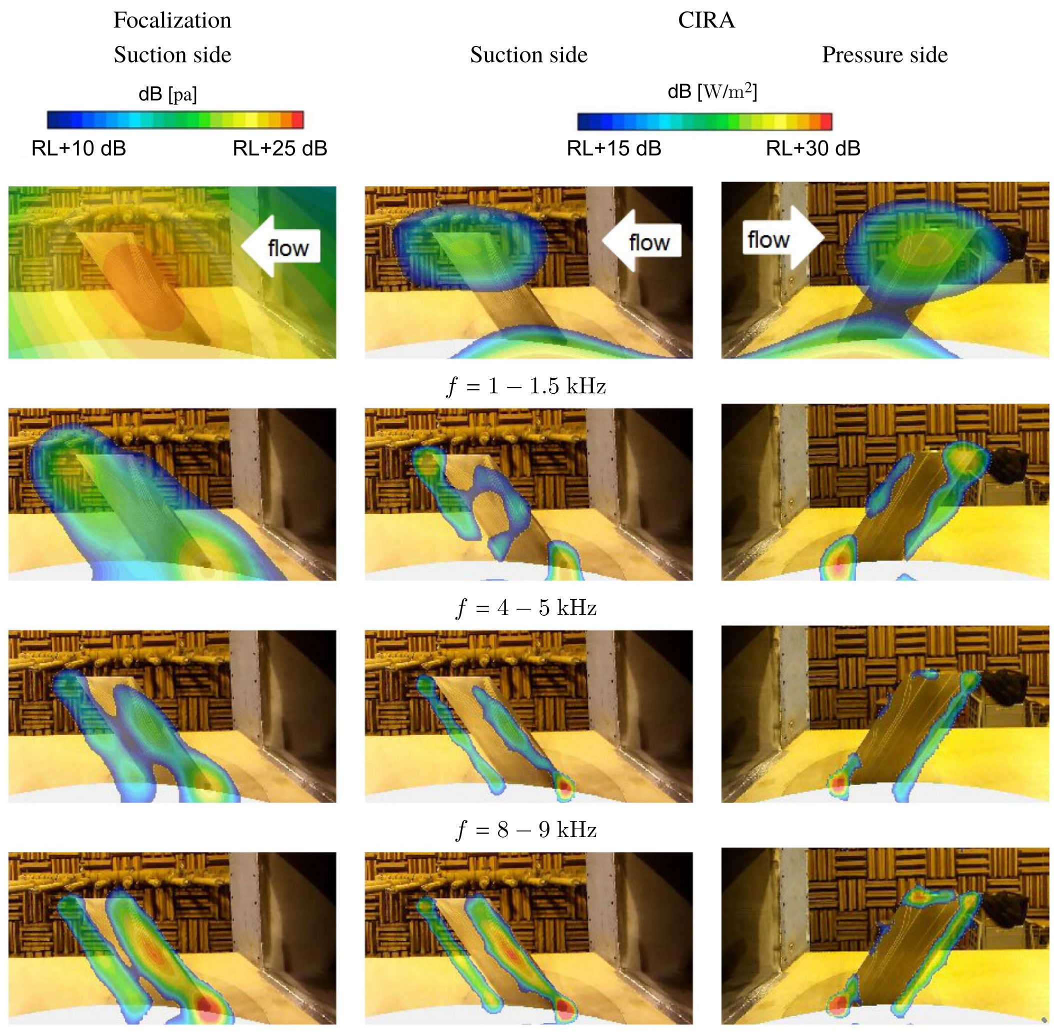

Fig. 7 Source-localization maps at $\alpha = 9$ deg and 90 m/s. Residual turbulence intensity is 0.5% (clean flow). Focalization and CIRA maps present source peak level contours and source intensity per unit area, respectively.

The focalization depicts source peak level contours, whereas the CIRA maps the source intensity per unit area. At low frequencies, the CIRA method performs much better to identify the noise source at the tip. This configuration also has noise sources at the junction, at the leading and trailing edges, and at the trailing-edge tip corner. The unexpected shift of the trailing-edge noise source as viewed from the suction side was observed despite wind-tunnel corrections, whereas the localization as viewed from the pressure side seems more accurate and reliable. This shift is most likely caused by the slight misalignment of the microphone array and the airfoil or the nozzle exit.

The scanned plane was subdivided into eight zones: four for the leading–edge (LE) area and four for the trailing-edge (TE) area, as shown in Fig. 8 by the rectangular boxes. If the noise source is the same for several zones (e.g., zones LE2, LE3, and LE4, including the leading-edge vortex in Fig. 8), then the recombined spectrum was calculated. This allows analyzing of the contribution of each source in the airfoil self-noise configuration, presuming that each zone is dominated by only one source, by comparing the associated pressure spectra.

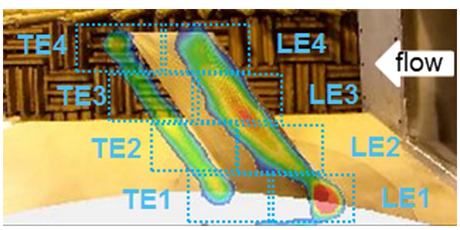

Fig. 8 Picture of swept airfoil and localization map. Zones for extraction of SPL. Nozzle exit is on right. Airfoil at $\alpha = 9$ deg and 90 m/s. Residual turbulence intensity is 0.5%.

For the CIRA algorithm, the following formula is used to convert the sound power levels (SWLs) produced by the localization algorithm into sound pressure levels (SPLs) in decibels:

$$L_p = \tilde{s}_{pp} - 10\log_{10}\left(\frac{A}{A_0}\right) \tag{18}$$

where L_p is the SPL, $\tilde{s}_{pp}$ is the SWL computed from the diagonal of matrix $\tilde{S}_{qq}$ in Sec. III.B, $A = 4\pi R^2$ is the area of the sphere of radius $R = 2$ m (distance from the airfoil to the far-field microphone in the present case), and A_0 is the reference area of 1 m^2.

Equation (18) is an approximation because propagation effects are not included: flow convection, reflection on the mounting plate, and nozzle diffraction. Moreover, the CIRA method does not provide estimates of the source directivity, other than the one encoded in the model matrix H. The CIRA technique assumes equivalent monopoles as sources, whereas the true sources have a dipole directivity. Even though the array is far enough from the angular range of extinction of the dipoles (chordwise place), this could produce small errors due to the different wave fronts of the true sources and of the assumed monopoles.

Figure 9 compares the obtained SPL spectra for each source, the total recombined spectrum (black line), and the spectrum measured

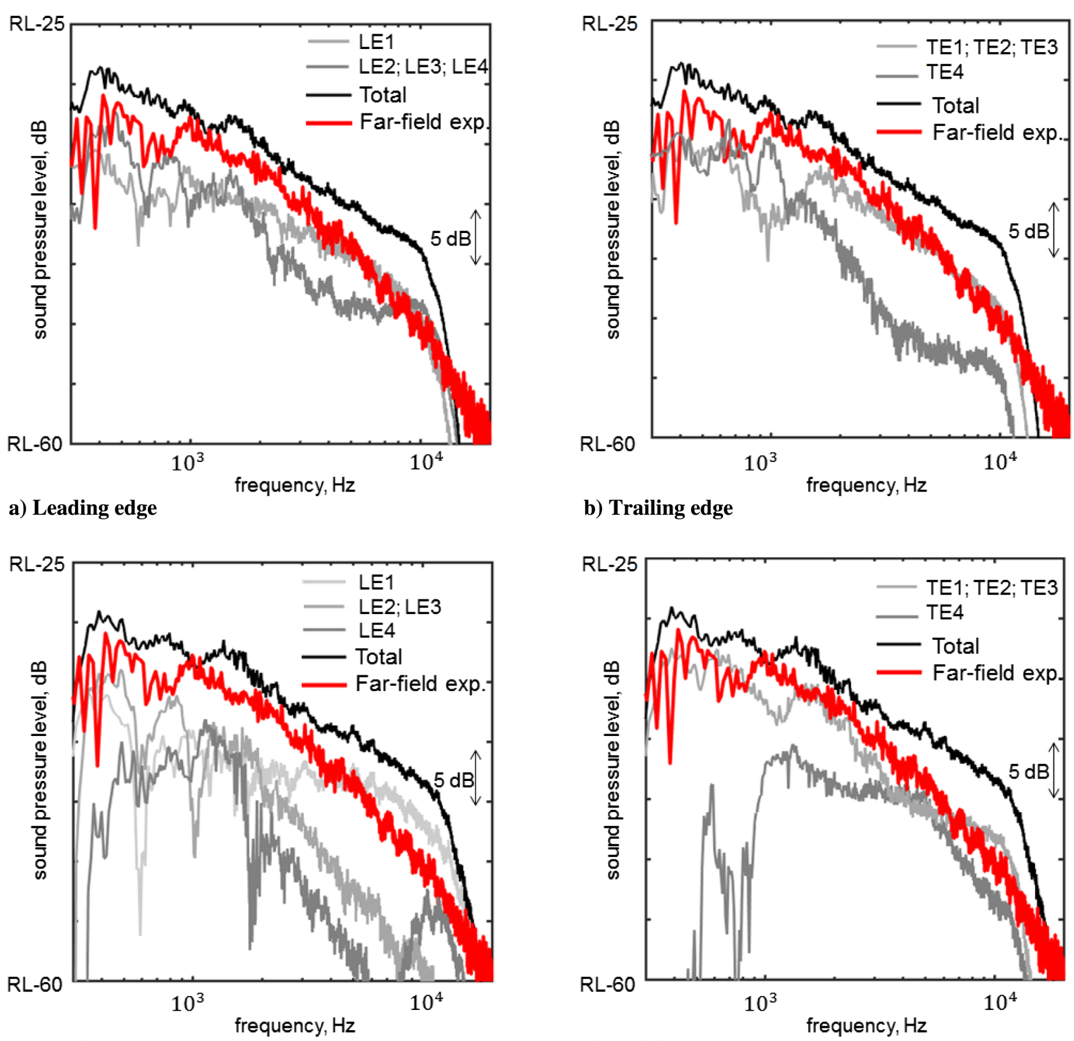

Fig. 9 SPL spectra for eight zones on a,b) suction side and on c,d) pressure side produced by CIRA method. Airfoil at $\alpha = 9$ deg and 90 m/s. Residual turbulence intensity is 0.5% (exp. = experimental).

by the single far-field microphone spectrum (red line) after extraction of the background noise. The spectral levels are corrected to a common distance. On the suction side, zone LE1 corresponds to the junction source; zones LE2, LE3, and LE4 include the leading-edge vortex; zone TE4 fits the trailing-edge tip source; and TE1, TE2, and TE3 cover the trailing-edge source. On the pressure side, the leading-edge tip noise is separated by zone LE4 so that zones LE2 and LE3 correspond to the part of the airfoil without significant noise generation. Other noise sources are similar to the ones on the suction side. The recombined spectrum of all zones produced by the CIRA method overestimates the measured far-field spectrum by a couple of decibels. The differences at higher frequencies around 10 kHz are more than 5 dB.

At frequencies beyond 2 kHz, the source at the junction (zone LE1) dominates for both sides of the array. For the pressure side, the trailing-edge tip contributes at frequencies from 2.5 to 6 kHz. Trailing-edge noise as viewed from this side is more significant than leading-edge noise.

An interesting feature is the imbalance between sounds radiated at high frequencies (typically in the range of 10–13 kHz) from the leading-edge area on the suction side and on the pressure side. This suggests that the source is not exactly at the edge, as what would be the case for turbulence interaction. In fact, this behavior is attributed to the formation of a leading-edge vortex that separates from the leading edge and reattaches slightly farther downstream on the suction side [3,4]. This leading-edge vortex noise is shielded by the blade, and consequently lower levels are observed on the pressure side.

Figure 10 presents localization maps from the array facing the suction side of the airfoil at $\alpha = 4$ deg and 90 m/s. A source at the trailing-edge tip corner is clearly found in this case at frequencies from 13 to 20 kHz, caused by a probable interaction of the unsteady tip vortex with this part of the surface. The unsteady Reynolds-averaged Navier–Stokes (uRANS) simulations provided by Quaglia [47] also show that the leading-edge vortex and the tip vortex merge in this place.

Figure 11 shows SPL spectra for the same case. The far-field spectrum is again overestimated by the reconstruction, as in the previous case (about 5 dB differences). It is worth noting that both measured and reconstructed far-field spectra exhibit a high hump at

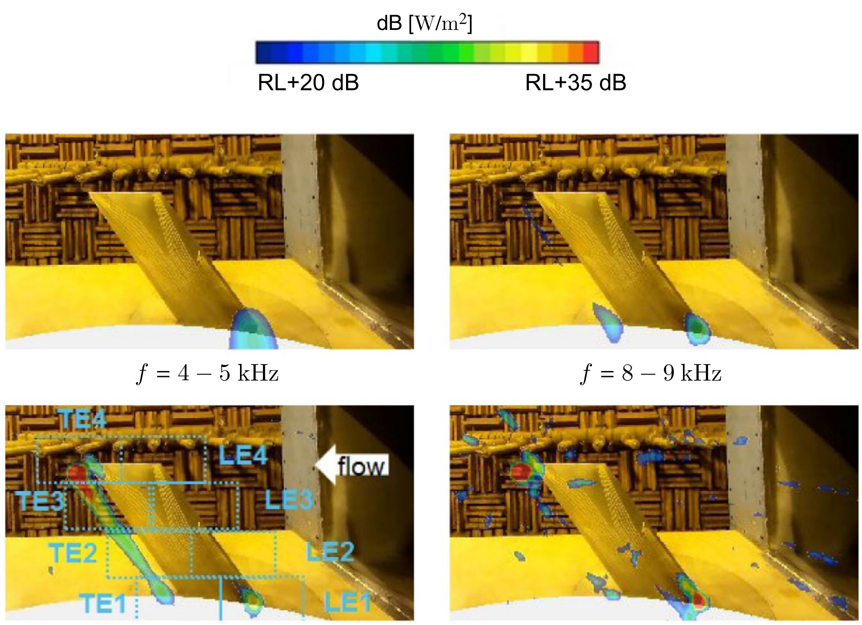

$f = 4 - 5$ kHz
$f = 8 - 9$ kHz
$f = 10 - 13$ kHz
$f = 13 - 20$ kHz

Fig. 10 Source-localization maps at $\alpha = 4$ deg and 90 m/s. Residual turbulence intensity is 0.5%, with CIRA, and suction-side view.

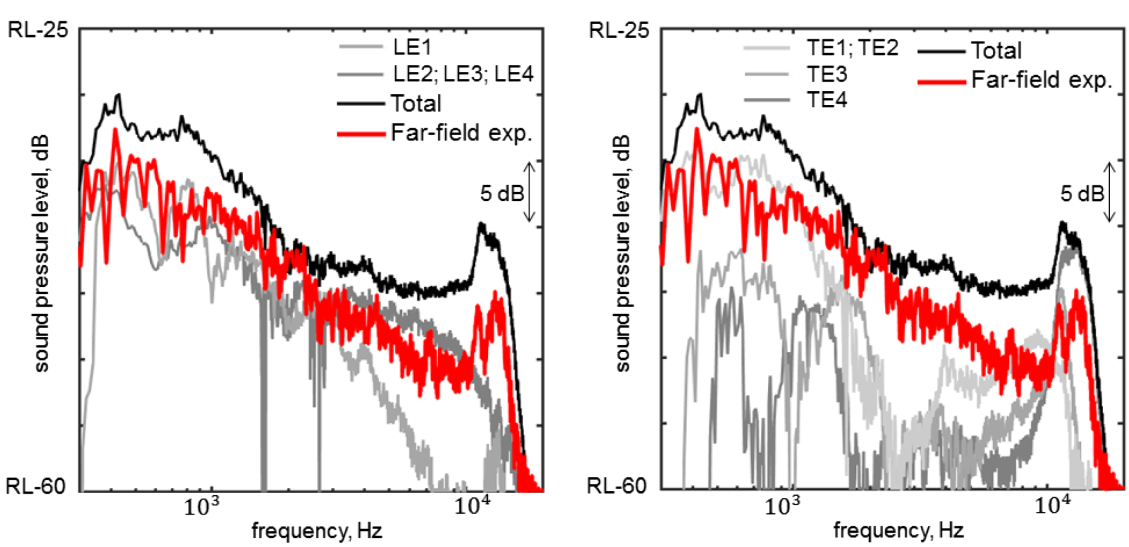

a) Leading edge **b) Trailing edge**

Fig. 11 SPL spectra for eight zones on suction side produced by CIRA method. Airfoil at $\alpha = 4$ deg and 90 m/s. Turbulence intensity is 0.5%.

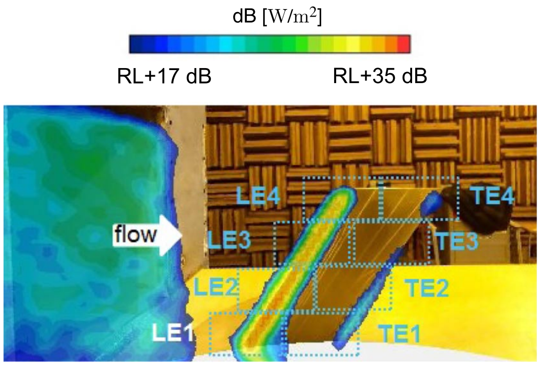

Fig. 12 Source-localization map at $\alpha = 9$ deg and 90 m/s calculated with CIRA method. Residual turbulence intensity is 8%. Frequency range from 10 to 13 kHz.

frequencies from 10 to 16 kHz. The hump of the directly measured spectrum is, however, more clearly divided into two peaks. The zones TE4 and TE3 contribute to the first peak, whereas the second one fully corresponds to the TE4 zone (trailing-edge tip source).

Figure 12 presents the source-localization map for the airfoil at 9 deg and 90 m/s with a turbulence intensity of 8%. The clear turbulence-interaction noise is seen along the full leading edge. At high frequencies, a weak source along the trailing edge is also observed. Since there are only two sources, zones LE1, LE2, LE3, and LE4 are combined as well as zones TE1, TE2, TE3, and TE4. It is worth noting that the large-scale turbulence at the exit of the nozzle has a lower noise level than the turbulence-interaction noise. As was presented by Bampanis and Roger [48], if only turbulence-interaction noise is investigated, the unnecessary additional sources (at the trailing edge for instance) could be removed to highlight the investigated phenomenon.

Figure 13 presents SPL spectra for arrays facing the suction (Fig. 13a) and pressure (Fig. 13b) sides of the airfoil in the configuration at 9 deg and 90 m/s with the high turbulence intensity of 8%. At frequencies below 3 kHz, the differences are quite important; but now, the SPL calculated from the CIRA technique underestimates the measured far-field spectrum. At higher frequencies, a very good agreement is found, especially on the pressure-side position. In this case, the physics of the leading-edge vortex is probably overwhelmed by the incoming turbulence; and turbulence-interaction noise, which is known to be symmetrically radiated, clearly dominates.

The discrepancies at frequencies below 3 kHz can be associated with the assumption of the perfectly decorrelated sources made for the CIRA model. The correlation length of the pressure fluctuations

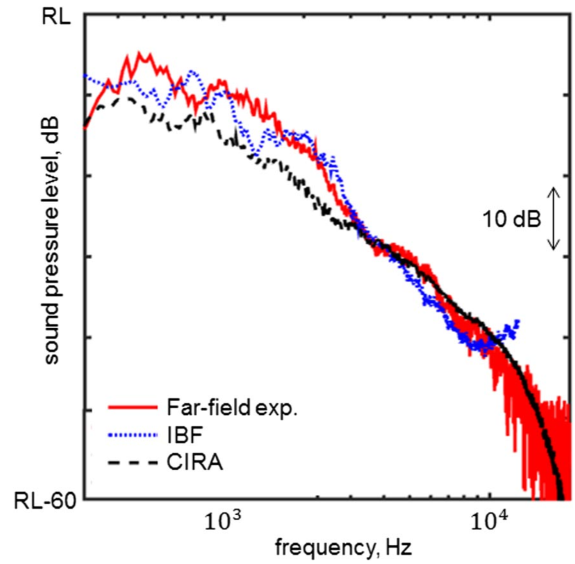

Fig. 14 Comparison of SPL spectra for airfoil at $\alpha = 9$ deg and 90 m/s. Residual turbulence intensity is 8%. Pressure side is shown.

at frequencies below 3 kHz reaches 0.02 m, whereas as was mentioned before, the cell size of the discretization mesh is 0.01 m. If a correction is applied in the range of positive values of the quantity in Fig. 6, a very good agreement is found over the entire frequency range. To avoid corrections associated with the correlation length, the iterative Bayesian focusing method [18] for which the sources are assumed to be partially correlated was used to improve the results. For the IBF algorithm, the following formula is used to compute the sound power level $\tilde{s}_{pp}$ at the far-field microphone position from the estimated source covariance matrix $\tilde{\boldsymbol{S}}_{qq}$:

$$\tilde{s}_{pp} = \boldsymbol{h}_{FF} \tilde{\boldsymbol{S}}_{qq} \boldsymbol{h}^*_{FF} \tag{19}$$

where $\boldsymbol{h}_{FF}$ is the $[1 \times N_s]$ propagation vector from the source point set to the far-field microphone using Eq. (5). This formulation includes source interference effects. The obtained spectrum (Fig. 14 blue line) is in a good agreement with the measured one (red line) starting from 1500 Hz. At high frequencies (from 8 kHz), the spectrum reconstructed with the IBF starts to increase. Overall, the Bayesian algorithm reduces the discrepancies from 10 to 5 dB compared with the CIRA method. The better agreement with the

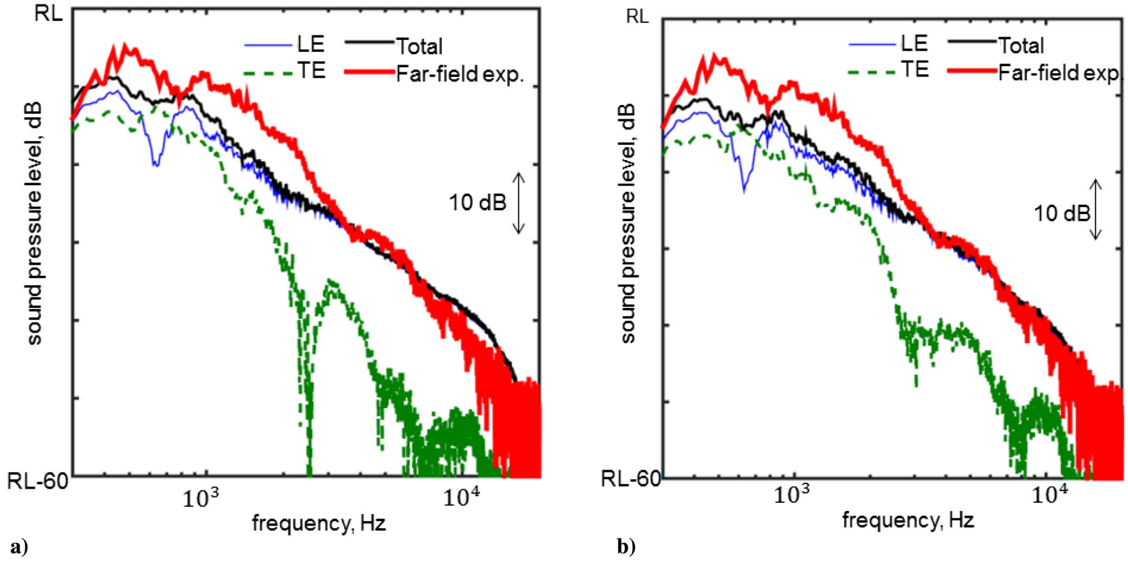

Fig. 13 SPL spectra for eight zones on a) suction side and on b) pressure side produced by CIRA method. Airfoil at $\alpha = 9$ deg and 90 m/s. Residual turbulence intensity is 8%.

measured spectrum may be linked to the ability of IBF to deal with source correlation, as presented in Sec. III.C. The low-frequency range of Fig. 12 is better predicted with this algorithm because turbulence-interaction noise is the main contributor and the discretization mesh spacing is lower than the associated coherence length $[\Delta x < \ell_y(f)]$. However, the low-frequency oscillations (below 1.5 kHz) of the IBF spectrum around the far-field measured spectrum indicate that source interferences are not perfectly accounted for. Some efforts are still needed for a better reproduction of these effects in the far field. A possible development is the introduction of prior information in the source correlation matrix.

VI. Conclusions

The present work is a detailed analysis of microphone-array measurements performed in a previously reported experimental investigation [3,4] initially dedicated to the turbulence-interaction noise of a cambered swept airfoil with a free tip in realistic loading conditions (freestream velocity of 90 m/s) typical of contrarotating open rotors. By placing the array on both sides of the airfoil outside of the deflected jet flow and by dividing the airfoil into eight localization zones, three main noise sources have been identified and quantified for the first time at a high angle of attack (9 deg): the diffraction at the trailing edge, the leading-edge vortex caused by sweep, and the tip vortex. Additionally, a noise source caused by a horseshoe vortex is evidenced at the junction between the holding plate and the airfoil.

Furthermore, because of the presence of several combined noise sources, the classical beamforming gives only qualitative results. Therefore, the cross-spectral matrix fitting method CIRA has been applied to produce more quantitative information. For each of the aforementioned zones, the contribution to the sound pressure level has been calculated as well as spectra for all zones. The total reconstructed spectra have been compared with the measured far-field spectra. A good overall shape agreement has been obtained, but either underestimates or overestimates of the far-field sound (differences around 10 dB) are observed with the reconstruction procedure. Without significant incoming turbulence, all the aforementioned sources contribute to the far-field noise at high frequencies (greater than 4 kHz). At midfrequencies, the trailing edge dominates. With 8% incoming turbulence, the leading-edge noise becomes dominant at all frequencies.

Some discrepancies are assumed to be caused by the uncorrelated source model used in the CIRA. To check this idea, the iterative Bayesian focusing algorithm has been used in which the correlation length is included. The obtained reconstructed spectrum has provided a better agreement with the measured one at midfrequencies (discrepancies around 5 dB). An analytical turbulence-interaction noise model confirmed that the discrepancies are related to correlation-length issues. This suggests that the array postprocessing still needs to be improved to provide accurate spectral information about extracted sources. Improvements to the basic source models and their correlation properties will be investigated during future work.

Acknowledgments

This work was performed within the framework of the Labex CeLyA of the Université de Lyon, within the program “Investissements d’Avenir” (ANR-10-LABX-0060/ANR-11-IDEX-0007) operated by the French National Research Agency (ANR) and is supported by the industrial Chair Aeroacoustics of Ducted and Open-rotor Propulsion SYStems (ADOPSYS) cofinanced by Safran Aircraft Engines and the ANR (ANR-13-CHIN-0001-01).

References

[1] Roger, M., and Moreau, S., “Broadband Self Noise from Loaded Fan Blades,” *AIAA Journal*, Vol. 42, No. 3, 2004, pp. 536–544. https://doi.org/10.2514/1.9108

[2] Moreau, S., and Roger, M., “Effect of Airfoil Aerodynamic Loading on Trailing Edge Noise Sources,” *AIAA Journal*, Vol. 43, No. 1, 2005, pp. 41–52. https://doi.org/10.2514/1.5578

[3] Giez, J., Vion, L., Roger, M., and Moreau, S., “Effect of the Edge and Tip Vortex on Airfoil Self Noise and Turbulence Impingement Noise,” *22nd AIAA/CEAS Aeroacoustics Conference*, AIAA Paper 2016-2996, May 2016. https://doi.org/10.2514/6.2016-2996

[4] Giez, J., Vion, L., Roger, M., Yakhina, G., and Moreau, S., “Effects of Intermittency and Geometry on the Turbulence Impingement Noise of a CROR Rear-Rotor Blade,” *23rd AIAA/CEAS Aeroacoustics Conference*, AIAA Paper 2016-3217, June 2017. https://doi.org/10.2514/6.2017-3217

[5] Wu, H., Sanjose, M., Moreau, S., and Sandberg, R. D., “Direct Numerical Simulation of the Self-Noise Radiated by the Installed Controlled-Diffusion Airfoil at Transitional Reynolds Number,” *2018 AIAA/CEAS Aeroacoustics Conference*, AIAA Paper 2018-3797, June 2018. https://doi.org/10.2514/6.2018-3797

[6] Johnson, D. H., and Dudgeon, D. E., *Array Signal Processing: Concepts and Techniques*, PTR Prentice–Hall, Englewood Cliffs, 1993, p. 252.

[7] Brooks, T. F., and Humphreys, W. M., “A Deconvolution Approach for the Mapping of Acoustic Sources (DAMAS) Determined from Phased Microphone Arrays,” *Journal of Sound and Vibration*, Vol. 294, Nos. 4–5, 2006, pp. 856–879. https://doi.org/10.1016/j.jsv.2005.12.046

[8] Sijtsma, P., “CLEAN Based on Spatial Source Coherence,” *International Journal of Aeroacoustics*, Vol. 6, No. 4, 2007, pp. 357–374. https://doi.org/10.1260/147547207783359459

[9] Bahr, C. J., Humphreys, W. M., Ernst, D., Ahlefeldt, T., Spehr, C., Pereira, A., Leclere, Q., Picard, C., Porteous, R., Moreau, D., et al., “A Comparison of Microphone Phased Array Methods Applied to the Study of Airframe Noise in Wind Tunnel Testing,” *23rd AIAA/CEAS Aeroacoustics Conference*, AIAA Paper 2017-3718, 2017. https://doi.org/10.2514/6.2017-3718

[10] Sarradj, E., Herold, G., Sijtsma, P., Merino Martinez, R., Geyer, T. F., Bahr, C. J., Porteous, R., Moreau, D., and Doolan, C. J., “A Microphone Array Method Benchmarking Exercise Using Synthesized Input Data,” *23rd AIAA/CEAS Aeroacoustics Conference*, AIAA Paper 2017-3719, 2017. https://doi.org/10.2514/6.2017-3719

[11] Geyer, T., Sarradj, E., and Giesler, J., “Application of a Beamforming Technique to the Measurement of Airfoil Leading Edge Noise,” *Advances in Acoustics and Vibration*, Vol. 2012, Feb. 2012, Paper 905461. https://doi.org/10.1155/2012/905461

[12] Shannon, D., and Morris, S. C., “Trailing Edge Noise Measurements Using a Large Aperture Phased Array,” *International Journal of Aeroacoustics*, Vol. 7, No. 2, 2008, pp. 147–176. https://doi.org/10.1260/147547208784649446

[13] Clark, I. A., Alexander, W. N., Devenport, W., Glegg, S., Jaworski, J. W., Daly, C., and Peake, N., “Bioinspired Trailing-Edge Noise Control,” *AIAA Journal*, Vol. 55, No. 3, 2016, pp. 740–754. https://doi.org/10.2514/1.J055243

[14] Moreau, J. D., Doolan, J. C., Alexander, N. W., Meyers, W. T., and Devenport, J. W., “Wall-Mounted Finite Airfoil-Noise Production and Prediction,” *AIAA Journal*, Vol. 54, No. 5, 2016, pp. 1637–1651. https://doi.org/10.2514/1.J054493

[15] Moreau, D. J., and Doolan, C. J., “Tonal Noise Production from a Wall-Mounted Finite Airfoil,” *Journal of Sound and Vibration*, Vol. 363, Feb. 2016, pp. 199–224. https://doi.org/10.1016/j.jsv.2015.11.021

[16] Brooks, T. F., and Marcolini, M. A., “Airfoil Tip Vortex Formation Noise,” *AIAA Journal*, Vol. 24, No. 2, 1986, pp. 246–252. https://doi.org/10.2514/3.9252

[17] Piet, J., and Elias, G., “Modélisation du Champ Acoustique Incident sur la Coiffe d’Ariane 5 par des Sources Simples,” Office National D’Études et de Recherches Aerospatiales Rept. TAP–94-062, Jouy-en-Josas, France, 1994.

[18] Antoni, J., “A Bayesian Approach to Sound Source Reconstruction: Optimal Basis, Regularization, and Focusing,” *Journal of the Acoustical Society of America*, Vol. 131, No. 4, 2012, pp. 2873–2890. https://doi.org/10.1121/1.3685484

[19] Humphreys, W., Shams, Q., Graves, S., Sealey, B., Bartram, S., and Comeaux, T., “Application of MEMS Microphone Array Technology to Airframe Noise Measurements,” *11th AIAA/CEAS Aeroacoustics Conference*, AIAA Paper 2005-3004, 2005. https://doi.org/10.2514/6.2005-3004

[20] Moreau, S., Roger, M., and Jurdic, V., “Effect of Angle of Attack and Airfoil Shape on Turbulence-Interaction Noise,” *11th AIAA/CEAS Aeroacoustics Conference*, AIAA Paper 2005-2973, 2005. https://doi.org/10.2514/6.2005-2973

[21] Paterson, R., and Amiet, R., “Acoustic Radiation and Surface Pressure Characteristics of an Airfoil due to Incident Turbulence,” *3rd Aeroacoustics Conference*, AIAA Paper 1976-0571, 1976. https://doi.org/10.2514/6.1976-571

[22] Devenport, W. J., Staubs, J. K., and Glegg, S. A., "Sound Radiation from Real Airfoils in Turbulence," *Journal of Sound and Vibration*, Vol. 329, No. 17, 2010, pp. 3470–3483.
https://doi.org/10.1016/j.jsv.2010.02.022

[23] Santana, L. D., Christophe, J., Schram, C., and Desmet, W., "A Rapid Distortion Theory Modified Turbulence Spectra for Semi-Analytical Airfoil Noise Prediction," *Journal of Sound and Vibration*, Vol. 383, Nov. 2016, pp. 349–363.
https://doi.org/10.1016/j.jsv.2016.07.026

[24] Amiet, R. K., "High Frequency Thin-Airfoil Theory for Subsonic Flow," *AIAA Journal*, Vol. 14, No. 8, 1976, pp. 1076–1082.
https://doi.org/10.2514/3.7187

[25] Roger, M., and Moreau, S., "Back-Scattering Correction and Further Extensions of Amiet's Trailing-Edge Noise Model. Part 1: Theory," *Journal of Sound and Vibration*, Vol. 286, No. 3, 2005, pp. 477–506.
https://doi.org/10.1016/j.jsv.2004.10.054

[26] Ffowcs Williams, J. E., and Hawkings, D. L., "Sound Generation by Turbulence and Surfaces in Arbitrary Motion," *Philosophical Transactions of the Royal Society of London, Series A: Mathematical and Physical Sciences*, Vol. 264, No. 1151, 1969, pp. 321–342.
https://doi.org/10.1098/rsta.1969.0031

[27] Quaglia, M. E., Léonard, T., Moreau, S., and Roger, M., "A 3-D Analytical Model for Orthogonal Blade-Vortex Interaction Noise," *Journal of Sound and Vibration*, Vol. 399, July 2017, pp. 104–123.
https://doi.org/10.1016/j.jsv.2017.03.023

[28] Moreau, S., and Roger, M., "Competing Broadband Noise Mechanisms in Low-Speed Axial Fans," *AIAA Journal*, Vol. 45, No. 1, 2007, pp. 48–57.
https://doi.org/10.2514/1.14583

[29] Leclère, Q., Pereira, A., Bailly, C., Antoni, J., and Picard, C., "A Unified Formalism for Acoustic Imaging Based on Microphone Array Measurements," *International Journal of Aeroacoustics*, Vol. 16, Nos. 4–5, 2017, pp. 431–456.
https://doi.org/10.1177/1475472X17718883

[30] Merino-Martinez, R., Sijtsma, P., Snellen, M., Ahlefeldt, T., Antoni, J., Bahr, C., Blacodon, D., Ernst, D., Finez, A., Funke, S., et al., "Aircraft Noise Generation and Assessment: A Review of Acoustic Imaging Methods Using Phased Microphone Arrays," *CEAS Aeronautical Journal*, Vol. 10, No. 1, 2017, pp. 197–230.

[31] Mueller, T. J. (ed.), *Aeroacoustic Measurements*, Springer–Verlag, Berlin, 2002, pp. 31–34.
https://doi.org/10.1007/978-3-662-05058-3

[32] Elias, G., "Experimental Techniques for Source Location," *Lectures Series 1997–07 Aeroacoustics and Active Noise Control*, von Kármán Inst. for Fluid Dynamics, Sint-Genesius-Rode, Belgium, Sept. 1997, p. 14.

[33] Sarradj, E., "Three-dimensional Acoustic Source Mapping with Different Beamforming Steering Vector Formulations," *Advances in Acoustics and Vibration*, Vol. 2012, June 2012, pp. 1–12.
https://doi.org/10.1155/2012/292695

[34] Blacodon, D., and Elias, G., "Level Estimation of Extended Acoustic Sources Using an Array of Microphones," *9th AIAA/CEAS Aeroacoustics Conference and Exhibit*, AIAA Paper 2003-3199, 2003.
https://doi.org/10.2514/6.2003-3199

[35] Yardibi, T., Li, J., Stoica, P., and Cattafesta, L. N., III, "Sparsity Constrained Deconvolution Approaches for Acoustic Source Mapping," *Journal of the Acoustical Society of America*, Vol. 123, No. 5, 2008, pp. 2631–2642.
https://doi.org/10.1121/1.2896754

[36] Elias, G., "Évaluation des Retards de Propagation Acoustique Adaptée à la Soufflerie Sources CEPRA 19," ONERA TR 38/3102 PN, Palaiseau, France, 1993.

[37] Schafer, R. W., Mersereau, R. M., and Richards, M. A., "Constrained Iterative Restoration Algorithms," *Proceedings of the IEEE*, Vol. 69, No. 4, 1981, pp. 432–450.
https://doi.org/10.1109/PROC.1981.11987

[38] Brooks, T., and Humphreys, W., "Extension of DAMAS Phased Array Processing for Spatial Coherence Determination (DAMAS-C)," *12th AIAA/CEAS Aeroacoustics Conference (27th AIAA Aeroacoustics Conference)*, AIAA Paper 2006-2654, 2006.
https://doi.org/10.2514/6.2006-2654

[39] Fleury, V., Bulte, J., and Davy, R., "Determination of Acoustic Directivity from Microphone Array Measurements Using Correlated Monopoles," *14th AIAA/CEAS Aeroacoustics Conference (29th AIAA Aeroacoustics Conference)*, AIAA Paper 2008-2855, 2008.
https://doi.org/10.2514/6.2008-2855

[40] Fleury, V., and Davy, R., "Large-Scale Jet Noise Testing, Reduction and Methods Validation" EXEJET": 5. Analysis of Jet-Airfoil Interaction Noise by Microphone Array Techniques," *20th AIAA/CEAS Aeroacoustics Conference*, AIAA Paper 2014-3036, 2014.
https://doi.org/10.2514/6.2014-3036

[41] Finez, A., Picard, C., Le Magueresse, T., Leclere, Q., and Pereira, A., "Microphone Array Techniques Based on Matrix Inversion," Von Karman Institute for fluid dynamics (VKI) Lecture Series STO-AVT-287, Sint-Genesius-Rode, Belgium, 2017.

[42] Suzuki, T., "L_1 Generalized Inverse Beam-Forming Algorithm Resolving Coherent/Incoherent, Distributed and Multipole Sources," *Journal of Sound and Vibration*, Vol. 330, No. 24, 2011, pp. 5835–5851.
https://doi.org/10.1016/j.jsv.2011.05.021

[43] Nelson, P. A., and Yoon, S.-H., "Estimation of Acoustic Source Strength by Inverse Methods: Part I, Conditioning of the Inverse Problem," *Journal of Sound and Vibration*, Vol. 233, No. 4, 2000, pp. 639–664.
https://doi.org/10.1006/jsvi.1999.2837

[44] Pereira, A., Antoni, J., and Leclere, Q., "Empirical Bayesian Regularization of the Inverse Acoustic Problem," *Applied Acoustics*, Vol. 97, Oct. 2015, pp. 11–29.
https://doi.org/10.1016/j.apacoust.2015.03.008

[45] Antoni, J., Le Magueresse, T., Leclère, Q., and Simard, P., "Sparse Acoustical Holography from Iterated Bayesian Focusing," *Journal of Sound and Vibration*, Vol. 446, 2019, pp. 289–325.
https://doi.org/10.1016/j.jsv.2019.01.001

[46] Le Magueresse, T., Minck, O., and Antoni, J., "Experimental Applications of Bayesian Focusing in an Industrial Context," *Proceedings of the ISMA 2018 Conference*, Katholieke Universiteit Leuven, Department of Mechanical Engineering, Leuven, Belgium, 2018, pp. 4389–4400.

[47] Quaglia, M., "Méthodes de Prévision Acoustique Semi-Analytiques pour un Doublet d'Hélices Contrarotatives Isolé," Ph.D. Thesis, Univ. of Sherbrooke, Sherbrooke, France, 2017.

[48] Bampanis, G., and Roger, M., "Three-Dimensional Effects in the Reduction of Turbulence-Impingement Noise of Aerofoils by Wavy Leading Edges," *Euronoise 2018 Crete*, EAA European Acoustics Assoc., 2018, pp. 97–104.

M. M. Choudhari
Associate Editor